PAPER

Check for updates

Benchmarks of the density functional tight-binding method for redox, protonation and electronic properties of quinones†

Maureen M. Kitheka, [a] Morgan Redington, [a] Jibo Zhang, [b] Yan Yao [b] and Puja Goyal ⋆[a]

Organic materials with controllable molecular design and sustainable resources are promising electrode materials. Crystalline quinones have been investigated in a variety of rechargeable battery chemistries due to their ubiquitous nature, voltage tunability and environmental friendliness. In acidic electrolytes, quinone crystals can undergo proton-coupled electron transfer (PCET), resulting in charge storage. However, the detailed mechanism of this phenomenon remains elusive. To model PCET in crystalline quinones, force field-based methods are not viable due to variable redox states of the quinone molecules during battery operation and computationally efficient quantum mechanical methods are strongly desired. The semi-empirical density functional tight-binding (DFTB) method has been widely used to study inorganic crystalline systems and biological systems but has not been comprehensively benchmarked for studying charge transport in quinones. In this work, we benchmark the third order variant of DFTB (DFTB3) for the reduction potential of quinones in aqueous solution, energetics of proton transfer between quinones and between quinones and water, and structural and electronic properties of crystalline quinones. Our results reveal the deficiencies of the DFTB3 method in describing the proton affinity of quinones and the structural and electronic properties of crystalline quinones, and highlight the need for further development of the DFTB method for describing charge transport in crystalline quinones.

Introduction

The exploration and utilization of renewable energy resources has steadily increased over the last few decades. The intermittent nature of these resources requires efficient energy storage technologies.[1] Lithium-ion batteries have been especially successful in this regard due to their high output voltage (3.5 V), high energy density (150–250 W h kg^{-1}), and good cycle stability. However, present day rechargeable batteries and supercapacitors utilize large amounts of transition metal oxides. Besides the environmental issues associated with these materials, their high cost and limited reserves have driven researchers to explore more environmental-friendly and low-cost materials for use in energy storage devices.

Organic electrode materials can be obtained directly or indirectly from natural renewable sources. The ability to design their structure flexibly allows convenient tailoring of their physical and electrochemical properties. In addition, they are generally not limited by the choice of counterions, increasing their attractiveness for energy storage device applications.[2–6] In 1969, Williams *et al.* made the first attempt to use an organic material, dichloroisocyanuric acid, in batteries.[7] After a hiatus in this research area due to issues related to high solubility and low doping level of organic materials, research in this field has picked up pace in the last few decades due to environmental issues. Quinones are especially interesting because of a variety of reasons: (a) high specific capacity, (b) high-rate capability due to fast redox kinetics, (c) long-term cycle stability due to structural stability, (d) ability to coordinate with univalent, divalent and even trivalent ions, (e) high electrochemical reversibility, and (f) diverse molecular structural design. Even the simplest quinone, 1,4-benzoquinone (BQ), can yield a theoretical specific capacity close to 496 mA h g^{-1} at a redox potential of ∼2.8 V *vs.* Li/Li$^+$, leading to an energy density far superior to that of conventional inorganic cathode materials.

Quinone-based electrode materials have been used in lithium, sodium, zinc, potassium, and magnesium ion batteries, supercapacitors, aqueous rechargeable batteries *etc.*[2–6,8–12] However, certain aspects of quinone-based electrode materials have been found to be less than ideal. (1) Small

a Department of Chemistry, State University of New York at Binghamton, Binghamton, NY 13905, USA. E-mail: pgoyal@binghamton.edu
b Department of Electrical and Computer Engineering and Texas Center for Superconductivity at the University of Houston, Houston, Texas 77024, USA

molecule quinones are highly soluble in aprotic electrolytes, particularly organic carbonate solvents generally used in lithium-ion batteries/sodium-ion batteries. This leads to low coulombic efficiency and rapid capacity fading. (2) Because they are light-weight, organic electrodes show low tap density, reducing the volumetric performance of the electrode. (3) Quinones generally have low intrinsic electrical conductivity, which lowers the practical specific capacity and limits the high rate charge/discharge performance.

Several practical strategies to overcome the above limitations of quinone-based electrodes have been devised. Molecular engineering, electrode design, electrolyte optimization, binder/separator modification, *etc.* have been attempted to overcome the dissolution issue. To increase the electrical conductivity, use of conductive additives, introduction of conductive moieties into the molecular structure, and immobilization of quinones on conductive matrices have been carried out. However, much remains to be understood about the fundamental mechanism of charge transport through crystalline quinones, quinone polymers, or quinones immobilized on conductive matrices so that better optimization of battery performance parameters can be achieved. Unlike lithium-ion batteries and aqueous rechargeable batteries for which both experimental and computational mechanistic studies abound, such studies hardly exist for batteries with quinone-based electrodes.

In acidic environments, quinones can undergo proton-coupled electron transfer (PCET) to form hydroquinones and this property allows them to store charge when they are used as electrode material in batteries with acidic electrolytes. Quite recently, several impressive studies on quinone-based "proton batteries" have been reported in the literature.[11–14] These batteries have either one or both electrodes comprised of quinones in some form, with the quinone molecules undergoing PCET. Liang *et al.*[11] found pyrene-4,5,9,10-tetrone (PTO) to be a very promising candidate for anode material due to the presence of four redox-active carbonyl groups and very low solubility in acid electrolyte. With a PTO anode and a PbO_2 cathode in 4.4 M H_2SO_4, they achieved a battery voltage of 1.27 V, specific capacity of 395 mA h g^{-1}, specific energy of 76 W h kg^{-1}, energy density of 161 W h l^{-1} and cycling stability of 96% over 1500 cycles/1200 h. However, in neutral and alkaline environments, they found PTO to have relatively higher solubility and used polymeric anode material. In a later study, using a PTO anode with a MnO_2-based cathode in an acidic electrolyte, Guo *et al.*[12] were able to attain an energy density up to 132.6 W h kg^{-1}, a power density of 30.8 kW kg^{-1}, and cycling stability over 5000 cycles. Their battery worked well even with a frozen electrolyte below −40 °C, and maintained superior rate performance and cycle stability even at −70 °C. They proposed the involvement of hydronium ions rather than protons as positive charge carriers in quinone crystals in the presence of acid electrolytes.

Batteries that employ quinone-based conducting redox polymers (CRPs) as electrode material have also been reported. Strietzel and co-workers[15] reported the design of an organic aqueous proton battery comprised of trimeric thiophene units

functionalized with quinones. The battery showed rapid charging and functioned even at temperatures as low as −248 °C. However, the voltage (0.4 V) and capacity (60 mA h g^{-1}) still needed improvement. In a subsequent study from the same group, Wang *et al.*[14] achieved a voltage of 0.8 V and a capacity of 62 mA h g^{-1} using quinizarin-CRP as the cathode, naphthoquinone-CRP as the anode, and a protic ionic liquid electrolyte.

The mechanism of PCET in crystalline quinones in batteries is largely unknown. For example, in crystalline PTO, the large O–O distances (~ 4 Å) between the PTO molecules point to large energy barriers for proton hopping between molecules, unless the proton transport involves water molecules, crystal distortions, or proton tunneling. However, it is not possible to elucidate the role of these aid factors using experiments alone. Density functional theory (DFT) has traditionally been the workhorse for computational mechanistic studies on batteries. However, a need for computationally more efficient methods exists. Such methods can allow comprehensive studies of ion transport mechanisms in quinone-based electrode materials, especially the role of crystal phase changes and of water in ion transport. They can also help to rapidly screen quinone-based materials based on calculated solubilities, band gaps (related to electrical conductivity), reduction potentials (related to battery voltage) *etc.* Methods derived from empirical force fields are not well-suited for modeling quinones in batteries due to the variable redox states of the quinone molecules during battery operation. Density functional tight-binding (DFTB),[16] a semi-empirical electronic structure method based on DFT which is about 1000 times faster than DFT, is very promising in this regard. However, since it is a semiempirical method, a detailed benchmarking of its performance for the actual system and the environment of interest is necessary. It has been widely used to study inorganic crystalline systems and biological systems in solution,[16] but has not been comprehensively benchmarked or parameterized for modeling charge transport in organic crystalline systems.

DFTB has been undergoing rapid continuing development. The DFTB+ software package allows parallel DFTB calculations on CPUs.[17] More recently, a heterogeneous CPU + GPU implementation of DFTB has been achieved and shown to enable simulations of entire proteins.[18] Nakai and co-workers have developed a divide and conquer scheme[19,20] for the efficient modeling of lithium-ion batteries. Several recent methodological developments, like the development of the DFTB3 method[21] and its corresponding parameterization,[22] the use of long-range corrections,[23] improvement of the description of intermolecular[24] and dispersion interactions,[25–28] have significantly increased the accuracy of the method. For parameterization, several automated schemes and schemes which utilize machine learning have been developed,[29–37] increasing the applicability of the DFTB method to different systems and problems.

With the long-term goal of understanding the charge transport mechanism in crystalline quinones in acidic battery environments where the positive charge carriers in the quinone electrode are protons, in this study, we benchmark the

This journal is © the Owner Societies 2022

Phys. Chem. Chem. Phys., 2022, **24**, 6742–6756 | **6743**

third-order variant of DFTB (DFTB3) with the 3OB parameter set (designed for DFTB3 as well as Organic and biological applications) for the (a) reduction potential of quinones, (b) energetics of proton transfer between quinones, and between quinones and water, (c) band structure/gap of crystalline quinones. The 3OB parameter set was developed for biological and molecular organic systems and it is interesting to examine its performance for crystalline organic systems. Wherever experimental data was unavailable, higher level electronic structure methods, mostly DFT, were utilized as reference. Several benchmarks involve PTO because of its promising behavior as electrode material in experimental studies.[2,8,10,11,38–45]

In this work, we investigate the accuracy of DFTB for the aforementioned properties. An outline of the paper is as follows. Section 2 describes the computational methodology used for the calculation of different properties. Section 3 presents the results, starting with the reduction potential, followed by proton transfer energetics and band structure/gap. Section 4 summarizes the insights obtained and provides concluding remarks. We conclude that DFTB3 with the 3OB parameter set provides a satisfactory description of the reduction potential of quinones in aqueous solution. It, however, shows significant errors in the energetics of proton transfer between quinone molecules at long O–O distances, and between quinones and water. The band structure and band gap from DFTB agree very well with those from the PBE density functional but are significantly different when compared to results with the HSE density functional. This work lays the foundation for future refinement of the DFTB method for the description of charge transport in crystalline quinone-based electrode material in batteries.
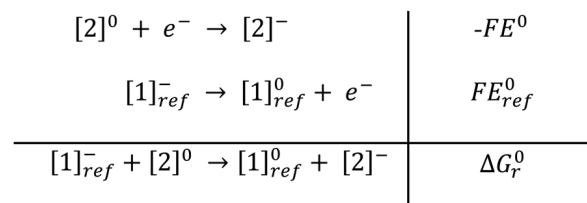
Methods

1. Reduction potential

The reduction potentials from DFT were used for benchmarking DFTB wherever experimental reduction potentials were not available. DFT calculations were carried out using the B3LYP[46] functional and the 6-31++G** basis set,[47] the combination of which has been previously benchmarked extensively for the reduction potential of quinones in implicit solvent and found to have excellent performance when compared to experiments.[48] The geometries were optimized in implicit water described using a conductor-like polarizable continuum model (CPCM)[49] and a similar protocol as in ref. 48. Test calculations with the IEFPCM model showed minimal change in the calculated reduction potentials (Table S1, ESI†). The reduction potentials were calculated using a reference reaction for error cancelation as shown in Scheme 1 and eqn (1).[48] All thermochemical data were calculated at 298.15 K. These calculations were carried out using the Gaussian 09 software package.[50]

$$E^0 = -\frac{\Delta G_r^0}{F} + E_{\text{ref}}^0 \qquad (1)$$

The reduction potential calculations with DFTB3 were carried out using implicit and explicit solvation models. For the explicit

$$[2]^0 + e^- \rightarrow [2]^- \qquad -FE^0$$

$$[1]_{\text{ref}}^- \rightarrow [1]_{\text{ref}}^0 + e^- \qquad FE_{\text{ref}}^0$$

$$[1]_{\text{ref}}^- + [2]^0 \rightarrow [1]_{\text{ref}}^0 + [2]^- \qquad \Delta G_r^0$$

Scheme 1 Scheme used for the calculation of reduction potentials using DFT. [2] is the species of interest and [1] is the reference species. E^0 and E_{ref}^0 are the reduction potentials of [2] and [1] respectively, with E_{ref}^0 known experimentally. ΔG_r^0 is the free energy of the redox reaction involving reduction of [2] and oxidation of [1]. F is the Faraday constant.

solvation model, the calculations were carried out in a hybrid quantum mechanical/molecular mechanical (QM/MM) framework using the thermodynamic integration (TI) methodology. The CHARMM program (version 40b1)[51] was used for these calculations. The neutral quinone molecule at its DFT-optimized geometry in implicit water was solvated in a cubic box of water molecules with the edge of the water box at least 15 Å distant from an atom in the quinone molecule. The water molecules were described using the modified TIP3P model in CHARMM[52] while the quinone molecule was described quantum mechanically using DFTB3 with the 3OB parameter set.[21,22] The Lennard-Jones parameters for the quinones were obtained from the CHARMM General Force Field (CGenFF).[53]

The 3OB parameter set for DFTB3 was used with the parameters listed in Table 1, where U^d are the Hubbard derivatives and W gives the spin constants. The tolerance for the change in energy between two consecutive self-consistent field (SCF) iterations was set at 10^{-7} kcal mol^{-1}.

In the TI calculations, the neutral quinone was assigned a value of zero for the coupling parameter, λ, while the reduced quinone was assigned a value of one for λ. The overall potential energy (U) of the system was calculated according to eqn (2), where U_Q and U_{Q^-} are the potential energy of the neutral and singly reduced quinone.

$$U = (1 - \lambda)U_Q + \lambda U_{Q^-} \qquad (2)$$

Six windows at λ values of 0.0, 0.2, 0.4, 0.6, 0.8 and 1.0 were used in TI. The solvated neutral quinone was used as the starting point for the calculations for the $\lambda = 1.0$ window. An initial minimization and equilibration for the $\lambda = 0.0$ and $\lambda = 1.0$ windows were first carried out since these corresponded to neutral and singly reduced quinone, respectively. Further simulation details are provided in the ESI.† The equilibrated structure from the $\lambda = 0.0$ window was used to initiate calculations for the $\lambda = 0.2$ and $\lambda = 0.4$ windows, while the equilibrated

Table 1 DFTB3/3OB parameters in atomic units, damping exponent $\zeta = 4.00$

Atom	U^d	Wss	Wsp	Wps	Wpp
H	−0.1857	−0.07174	0.0	0.0	0.0
C	−0.1492	−0.03062	−0.02505	−0.02505	−0.02265
O	−0.1575	−0.03524	−0.02956	−0.02956	−0.02785

structure from the $\lambda = 1.0$ window was used to start calculations for the $\lambda = 0.6$ and $\lambda = 0.8$ windows. For the 0.2, 0.4, 0.6 and 0.8 windows, an equilibration similar to the 0.0 and 1.0 windows was carried out. A 400 ps production run was subsequently carried out for all the λ windows. The energy gap $U_{Q^-} - U_Q$ was plotted as a function of time for each λ window to ensure proper equilibration (Fig. S1–S7 in the ESI†). The standard error in the average energy gap for each λ window was estimated using the block averaging method (Fig. S8–S14, ESI†). The average energy gap $U_{Q^-} - U_Q$ for each λ window was plotted as a function of λ. The plot was found to be linear in all cases (Fig. S15, ESI†). The Helmholtz reduction free energy (ΔF) was calculated using eqn (3),

$$\Delta F = \int_0^1 \left(\frac{\partial F}{\partial \lambda}\right)_\lambda d\lambda = \int_0^1 \langle U_{Q^-} - U_Q \rangle_\lambda d\lambda \qquad (3)$$

Using the linear fit, $\Delta F = \frac{m}{2} + c$, where m is the slope and c is the intercept. The reduction potential of the quinone of interest was calculated according to eqn (1) since the Gibbs reduction free energy can be approximated to be equal to the Helmholtz reduction free energy for a condensed phase reaction at constant volume and pressure.

For DFTB3 reduction potential calculations in implicit solvent, we used the conductor-like screening model (COSMO),[54] with the solvent accessible surface area (SASA) model for the non-electrostatic contributions. Bondi radii were used for all atoms.[55] The Hubbard derivatives, damping exponent and spin constants are listed in Table 1. Similar to the reduction potential calculations using DFT in implicit solvent, these calculations utilized Scheme 1 and eqn (1). Unlike the DFT reduction potential calculations in implicit solvent, no thermochemical data were included in the DFTB3 calculations in implicit solvent. These calculations were carried out using the DFTB+ software package (version 21.1).[17] The tolerance for the maximum change in any charge between two consecutive SCF iterations was set at 10^{-6} au. Additional test calculations in implicit solvent were carried out with two explicit water molecules hydrogen bonded to each carbonyl group of the quinones. These water molecules were treated quantum mechanically using DFTB3.

The effect of dispersion on calculated reduction potentials was also tested by comparing B3LYP to B3LYP-D3 and DFTB3 to DFTB3-D3.[56] In DFTB3-D3 calculations, Becke–Johnson damping[57] with values of 0.746, 4.191, and 3.209 au for the a_1, a_2 and s_8 dispersion parameters, respectively, was used.[58]

2. Proton transfer

DFT calculations were carried out using the M06[59] functional and the 6-31++G** basis set. MP2[60] with the aug-cc-pVDZ[61] basis set was used for one system to benchmark M06/6-31++G**. Semi-empirical calculations were carried out using DFTB3 with the 3OB parameter set.[21,22] The values of Hubbard derivatives, spin constants and the damping exponent were the same as specified in the reduction potential section. The tolerance for the maximum change in any charge between two SCF iterations was set at 10^{-7} au and 10^{-6} au for

calculations on BQ and PTO, respectively. Test calculations with DFTB3-D3 were also performed.

For proton transfer (PT) energy profiles involving PTO and water, relaxed scans in the gas phase were carried out using M06 and DFTB3. For the DFT calculations, a constraint was applied between a carbonyl oxygen atom of the PTO molecule and the transferring proton. For the DFTB3 calculations, optimizations were initiated from the DFT-optimized geometries and the O and H atoms involved in the reaction coordinate were frozen in space. A similar procedure was adopted for PT energy profiles involving two BQ molecules, except that in one set of calculations, the O–O distance between the neighboring carbonyl groups of the BQ molecules was kept fixed at 3.52 Å. The energy profile for PT between two PTO molecules at their crystal structure geometry, where the shortest intermolecular O–O distance was 4.0 Å, was also computed.

The PT between a neutral PTO molecule and a hydronium ion, and the PT between two neutral BQ molecules with the donor O-acceptor O distance fixed at 3.52 Å were also investigated with the PBE, B3LYP and ωB97XD functionals and the 6-31++G** basis set in the gas phase. For these two systems, calculations with the M06 functional and DFTB3 were also carried out in implicit solvent.

Proton affinities (PA) were computed with the G3B3[62] and DFTB3 methods using eqn (4). Zero-point corrections and thermal contributions were not included for either method. G3B3 is a variant of the Gaussian-3 (G3) theory[63] that involves geometry optimizations and zero point energy calculations using B3LYP/6-31G(d). Geometry optimizations are followed by single point energy calculations at the MP2, MP4 and QCISD(T) levels, the latter two with the frozen core approximation, for different components of the overall energy. It has been shown to perform very well for the calculation of proton affinities, among other properties like enthalpies of formation, ionization potentials and electron affinities.

$$PA = E^{H^+} + E^{B^-} - E^{BH} \qquad (4)$$

E^{H^+} is the energy of the proton and has a value of zero for DFT and a value of 151.04[21] kcal mol^{-1} for DFTB3. E^{B^-} and E^{BH} denote the energy of the deprotonated and protonated species, respectively. The DFT and DFTB3 calculations were carried out using the Gaussian 09 and DFTB+ (version 19.1)[64] software packages, respectively.

3. Band structure

DFT and DFTB3 calculations were carried out on crystalline PTO and BQ, both of which belong to the $P2_1/c$ space group. The PTO crystal structure will be reported separately[65] and the BQ crystal structure was obtained from the Cambridge Structural Database.[66] We used a generalized gradient approximation (GGA) functional, namely, Perdew–Burke–Ernzernhof (PBE),[67] and a Coulomb hybrid functional, namely, Heyd–Scuseria–Ernzernhof (HSE06),[68] to describe the electron–electron exchange and correlation interactions. The interactions between the core and valence electrons in our system were described using (1) the projector augmented wave (PAW)

method,[69] (2) the ultra-soft pseudopotential (USPP),[70] and (3) the optimized norm-conserving (ONCV) pseudopotential.[71] The PAW parameters utilized in this study were obtained from a standard solid state pseudopotential library (SSSP Efficiency).[72] For USPP, we used the Pslibrary 1.0.0[73] and for the ONCV PP, we used the SG15 library.[74] All DFT calculations were carried out using Quantum Espresso (QE) version 6.5.[75]

The PBE calculations were performed using a 60 Ry plane-wave cutoff and a dense Monkhorst–Pack uniform converged k-grid of $15 \times 3 \times 6$ and $6 \times 5 \times 5$ for PTO and BQ, respectively.[76] Finer $30 \times 6 \times 12$ and $12 \times 10 \times 10$ k-grids were used when computing the density of states for PTO and BQ, respectively. The k-path used in the band structure calculations for both DFT and DFTB3 methods was obtained from materialscloud.org[77] with high symmetry points from Γ (0,0,0) to Z (0,1/2,0), from Z (0,1/2,0) to D (0,1/2,1/2), from D (0,1/2,1/2) to B (0,0,1/2), from B (0,0,1/2) to Γ (0,0,0), from Γ (0,0,0) to A (−1/2,0,1/2), from A (−1/2,0,1/2) to E (−1/2,1/2,1/2), from E (−1/2,1/2,1/2) to Z (0,1/2,0), from Z (0,1/2,0) to C_2 (−1/2,1/2,0), from C_2 (−1/2,1/2,0) to Y_2 (−1/2,0,0), and from Y_2 (−1/2,0,0) to Γ (0,0,0). DFT geometry and lattice optimizations were carried out using the Broyden–Fletcher–Goldfarb–Shanno (BFGS) algorithm[78] with default values for the convergence threshold for total energy and forces.

DFTB3 geometry and lattice optimizations were carried out using the Conjugate Gradient (CG) algorithm[79] and the same DFTB3 parameters as provided in the reduction potential section. In some of the DFTB3 calculations on crystalline PTO and BQ, D3 dispersion corrections[56] were included using the same parameters as in the reduction potential and PT calculations.[57] The tolerance for the maximum change in any charge between two consecutive SCF iterations was set at 10^{-6} au. The optimization was stopped when the force component with the largest absolute value became lower than 10^{-4} au.

Calculations with the HSE06 functional used the optimized lattice-geometry obtained from the PBE/PAW method. We utilized the Wannier90 (version 3.1.0) code[80] to calculate the Maximally Localized Wannier Functions (MLWFs)[81] which were set to 132 and 56 for PTO and BQ with converged $4 \times 4 \times 4$ and $6 \times 6 \times 6$ Monkhorst–Pack k-grids, respectively. The number of

MLWFs was equal to the number of bands for each system, therefore the use of disentanglement parameters was not invoked. MLWFs were projected on the H s orbitals, C p orbitals and O p orbitals for both PTO and BQ since these were found to be the dominant contributing orbitals to the valence band (VB) and the conduction band (CB) near the Fermi level in the PBE and DFTB3 results. The sequence of calculations for all the methods is outlined in Table 2.

Results and discussion

1. Reduction potential

Several computational studies aimed at the high throughput computational screening of quinones based on their reduction potentials for use in redox flow batteries have been carried out.[82,83] Some fundamental studies on the mechanism of charge storage[84,85] and transport[86] in quinones have also been carried out, all based on DFT. Recent studies employed DFTB for gas phase geometry optimizations and DFT for subsequent single point energy calculations to calculate reduction potentials of quinones, and concluded DFTB to have good performance.[87,88] In the past, DFTB has been benchmarked for the reduction potential of several simple molecules and copper-containing transition metal complexes,[89–92] and was found to have modest accuracy with errors in most cases ranging from 100 to 200 mV. A more recent method similar to DFTB3, GFN2-xTB, has been benchmarked for the reduction potential of several organic and organometallic molecules and found to have similar accuracy as low-cost density functionals like B97-3c.[25,93] Here, we examine the performance of DFTB for the reduction potential of quinones in both implicit solvent and explicit solvent, the latter using a QM/MM framework and the TI methodology. Such an examination is directly relevant to our future dynamics studies of the charge transport mechanism in explicitly solvated quinone crystals.

1,4-Benzoquinone and 1,2-naphthoquinone were studied as reference molecules[20] for p-quinones and o-quinones, respectively. The main molecule of interest, PTO, was treated as a combination of two o-quinones. Hence 1,2-naphthoquinone

Table 2 Description of the steps involved in computing the band structure for crystalline quinones

| PBE	DFTB3/3OB	HSE06
Benchmark of k-points at a plane wave cutoff of 60 Ry		Benchmark of k-points at a plane wave cutoff of 60 Ry
SCF calculation using a $15 \times 3 \times 6$ k-grid		SCF calculation using a $4 \times 4 \times 4$ k-grid
Non-SCF calculation using a $30 \times 6 \times 12$ k-grid to obtain the density of states (DOS)	Utilization of the k-points obtained from the non-SCF calculation step in PBE to obtain the DOS	
		Use of the open_grid.x code in QE to unfold the k-grid obtained from the SCF calculation
Band structure calculation using Γ–Z–D–B–Γ–A–E–Z–C_2–Y_2–Γ as the k-path	Band structure calculation using the same k-path as PBE	Utilization of the Wannier90 (v3.1.0) code to obtain the MLWFs; band structure calculation using the same k-path as PBE
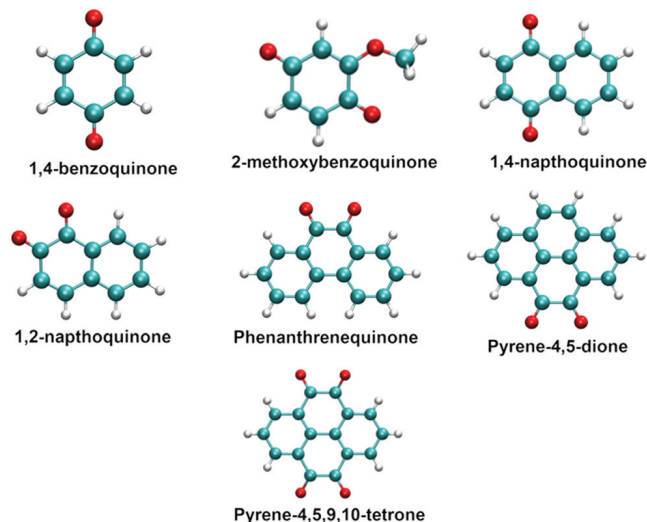
Fig. 1 A pictorial representation of the quinones used in reduction potential calculations. The atoms in red, cyan, and white represent oxygen, carbon, and hydrogen, respectively.
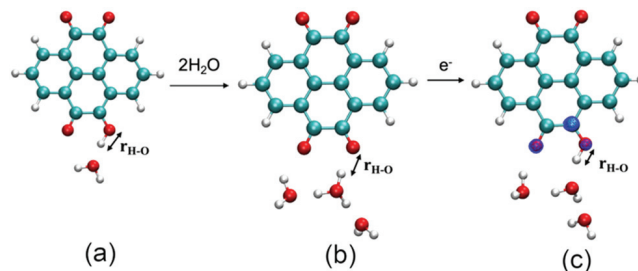

Fig. 2 Depiction of the reaction coordinate (r_{H-O}) for the study of proton transfer between (a) PTO and water, (b) PTO and a cluster of water molecules, (c) singly reduced PTO and a cluster of water molecules. The blue mesh represents the spin density isosurface (isovalue used was 0.02 Bohr^{-3}).

was used as a reference for PTO. Fig. 1 depicts all the quinones employed here for reduction potential studies. 2-methoxy-benzoquinone and 1,4-napthoquinone were used as examples of *p*-quinones, and phenanthrenequinone and pyrene-4,5-dione were used as examples of *o*-quinones. The B3LYP/6-31++G** method has been benchmarked extensively for the reduction potential of quinones in implicit solvent and found to yield results close to experiments.[48] We hence use B3LYP/6-31++G** reduction potential data to gauge the accuracy of DFTB3 reduction potentials in both implicit and explicit solvent whenever experimental data is missing.

Table S2 (ESI†) shows that compared to quinones in only implicit solvent, the additional inclusion of a few explicit water molecules hydrogen bonded to the carbonyl groups and treated quantum mechanically changes the reduction potential by only 6–12 mV (0.1–0.3 kcal mol^{-1}). Compared to quinones in only explicit solvent treated using molecular mechanics and periodic boundary conditions, a few explicit water molecules treated quantum mechanically and immersed in implicit water changes the reduction potential by only 37-71 mV (0.8-1.6 kcal mol^{-1}). We hence conclude that treating the explicit water molecules close to the quinone quantum

mechanically makes negligible difference to the calculated reduction potential. Therefore, the treatment of all water molecules in the QM/MM TI calculations using the modified TIP3P water model is a reasonable approximation.

Table S3 (ESI†) shows that dispersion has minimal effect on the reduction potential values from both DFT and DFTB3. When additional explicit QM water molecules hydrogen bonded to the carbonyl groups are included in the implicit solvent calculations, the effect of dispersion is slightly more pronounced than when only a QM quinone is studied in implicit solvent. The effect is however still very small.

As shown in Table 3, the calculated reduction potentials are generally in the order DFT > DFTB3 implicit > DFTB3 explicit. However, when compared to DFT, DFTB3 underestimates the reduction potentials only by less than ~2.5 kcal mol^{-1}. For the *p*-quinones, all three methods predict the reduction potentials to be in the order MBQ > 1,4-NQ. For the *o*-quinones, all three methods predict the reduction potentials to be in the order PTO > PQ > PDO. We conclude that not only in an implicit solvent framework but also in a QM/MM framework with explicit solvent and the TI methodology, DFTB provides a sufficiently accurate description of the reduction potential of quinones, making it useful for studying charge transport in quinones in an explicitly modeled condensed phase environment.

2. Proton transfer

DFTB has been used extensively to study PT in chemical and biological systems.[94–106] Several methodological developments

Table 3 Reduction potentials of selected quinones(v)^a

Quinone	Exp.^{b}	B3LYP/6-31++G** implicit	DFTB3/3OB implicit^c	DFTB3/3OB explicit^c
p-quinones				
1,4-benzoquinone (BQ)	0.099			
2-methoxybenzoquinone (MBQ)		−0.039^b	−0.114 (−0.075)	−0.145 (−0.106)
1,4-napthoquinone (1,4-NQ)	−0.140	−0.175	−0.188 (−0.013)	−0.271 (−0.096)
o-quinones				
1,2-napthoquinone (1,2-NQ)	−0.089			
Phenanthrenequinone (PQ)	−0.124	−0.218	−0.265 (−0.047)	−0.300 (−0.082)
Pyrene-4,5-dione (PDO)		−0.228	−0.305 (−0.077)	−0.342 (−0.114)
Pyrene-4,5,9,10-tetrone (PTO)		0.021	0.123 (0.101)	−0.009 (−0.030)

^{a} BQ and 1,2-NQ were used as reference molecules. ^{b} Ref. 48. ^{c} Numbers in parentheses represent the errors in DFTB3 relative to DFT.
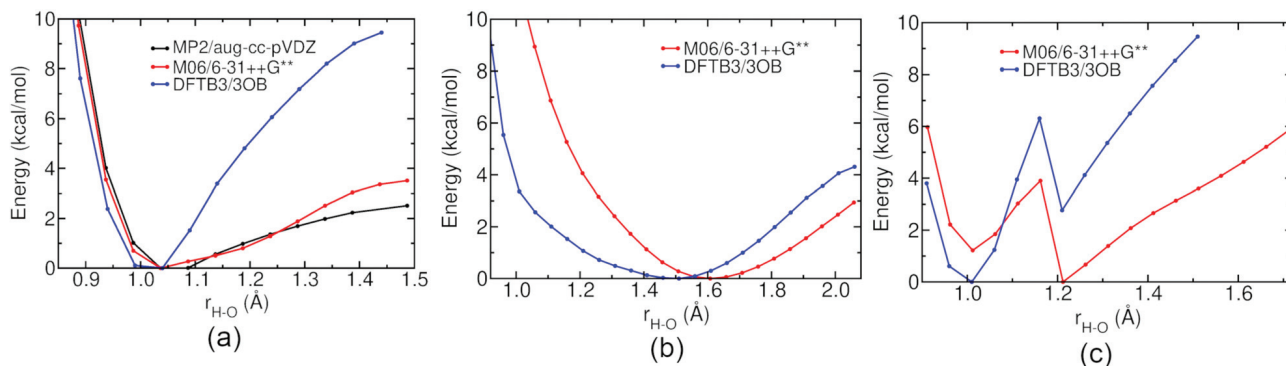
Fig. 3 Comparison of MP2, DFT and DFTB methods for proton transfer energetics along the H–O reaction coordinate (Fig. 2) in (a) PTO + H_3O^+, (b) PTO + H_3O^+ + $2H_2O$, (c) PTO + H_3O^+ + $2H_2O$ + e^-.

in DFTB over the years, including modification of the O–H repulsive potential, inclusion of third order terms in the Taylor series expansion and re-parameterization, have enhanced its accuracy for modeling PT.[21,22,95,98] However, the description of the energetics of PT between quinone molecules or between quinones and water by DFTB has not been investigated. Here, we carry out such an investigation using a combination of PT energy profiles and PA calculations.

For PT involving PTO and water (Fig. 2), the following three scenarios were considered: (a) neutral PTO hydrogen bonded to a hydronium ion, (b) neutral PTO hydrogen bonded to a hydronium ion stabilized by two other water molecules, (c) same as (b) but with an additional electron. For PT between PTO and a hydronium ion (Fig. 3a), MP2 and M06 show good agreement in terms of energetics with the M06 energy being only ~1.0 kcal mol^{-1} higher than the MP2 energy when the proton is localized on water. In all other PT calculations, M06/6-31++G** is used as the reference for gauging the accuracy of DFTB3.

For case (a), MP2, M06 and DFTB3 show good agreement in the position of the energy minimum (Fig. 3a). This corresponds to the localization of the proton on the quinone. However, DFTB3 overestimates the stabilization of the proton on the quinone by about 6 kcal mol^{-1} when compared to M06. For case (b), the addition of two water molecules next to the water molecule hydrogen bonded to PTO favors the formation of the hydronium ion (Fig. 3b). However, DFTB3 underestimates the PTO–proton distance at the energy minimum and overestimates the stabilization of the proton on PTO. In the presence of an additional electron in case (c), where the unpaired electron is found to be delocalized across the two PTO carbonyl groups next to the water molecules (Fig. 2c), M06 predicts two minima along the PT energy profile (Fig. 3c). The global minimum corresponds to proton sharing between PTO and water and the other minimum corresponds to the protonation of PTO. M06 predicts the global minimum to be ~1 kcal mol^{-1} lower in energy than the local minimum. On the other hand, DFTB3 predicts the protonated PTO geometry to be the global minimum and ~2 kcal mol^{-1} lower in energy than the shared proton geometry. Overall, from the PT energy profiles, DFTB3 is found to overestimate the stabilization of the proton on PTO.

Table 4   Proton Affinities in kcal mol^{-1}: deviation of DFTB3 in comparison to G3B3[a]

Molecule	G3B3	DFTB3/3OB
o-BQ	204.0	+6.8
p-BQ	196.5	+10.1
o-BQ$^{\bullet-}$	344.0	+6.8
p-BQ$^{\bullet-}$	330.9	+7.9

[a] Species in the table are reported in the unprotonated form.

Table 4 shows that for both o-BQ and p-BQ, irrespective of whether BQ is neutral or singly reduced, DFTB3 overestimates the proton affinity by ~7–10 kcal mol^{-1}. According to ref. 21, DFTB3/3OB overestimates the proton affinity of a water molecule by 1.5 kcal mol^{-1} and underestimates the proton affinity of a cluster of three water molecules by 2.5 kcal mol^{-1} when compared to G3B3. This indicates that the errors in the proton transfer energy profiles with DFTB3 are largely because of the inability of DFTB3/3OB to describe the proton affinity of quinones accurately. These errors reveal the deficiencies in the existing DFTB3 parameterization for modeling PT between quinones and water.

To understand the errors when studying PT between two quinone molecules (Fig. 4a and 5a), we first considered PT between two neutral BQ molecules and between two BQ radical anions with the donor O-acceptor O distance allowed to change freely. For PT between the neutral molecules, M06 predicts proton delocalization and proton sharing, with the cost of proton localization being only ~2 kcal mol^{-1} (Fig. 4b). DFTB3 slightly underestimates the cost of proton localization by ~1.5 kcal mol^{-1}. For PT between the singly reduced molecules, M06 and DFTB3 agree very well and predict the proton to be delocalized between the two quinone molecules (Fig. 4c). Fig. S16 (ESI†) shows dispersion to have minimal effect on this PT energy profile. PT between two neutral BQ molecules with the donor O-acceptor O distance fixed at 3.52 Å was found to have a large barrier of ~50 kcal mol^{-1} with M06 (Fig. 4d). DFTB3 was found to underestimate this barrier by ~8 kcal mol^{-1}.

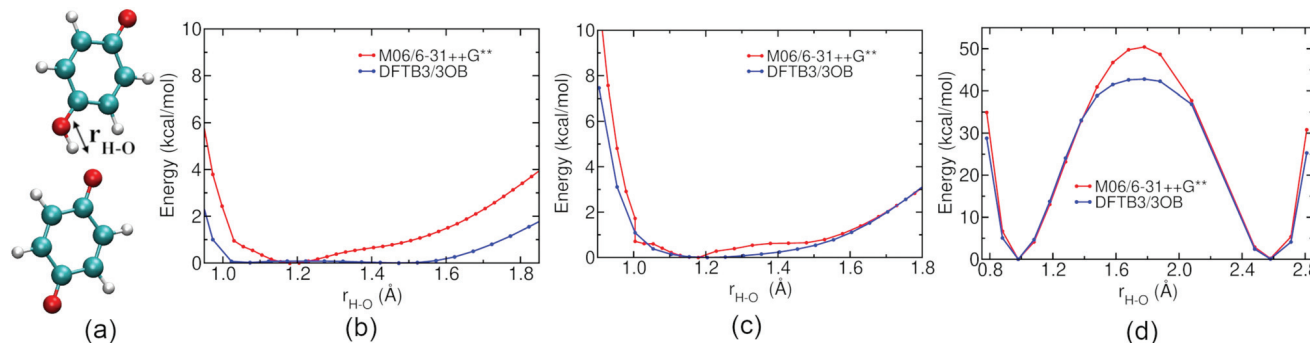The underestimation of the PT barrier between quinones at large O–O distances by DFTB3 was confirmed by calculations of

Fig. 4 (a) Depiction of the reaction coordinate (r_{H-O}) for the study of proton transfer between benzoquinone molecules, (b) energy profile for proton transfer between two neutral BQ molecules with the donor O-acceptor O distance allowed to change freely, (c) energy profile for proton transfer between two BQ radical anions with the donor O-acceptor O distance allowed to change freely, (d) energy profile for proton transfer between two neutral BQ molecules with the donor O-acceptor O distance fixed at 3.52 Å.
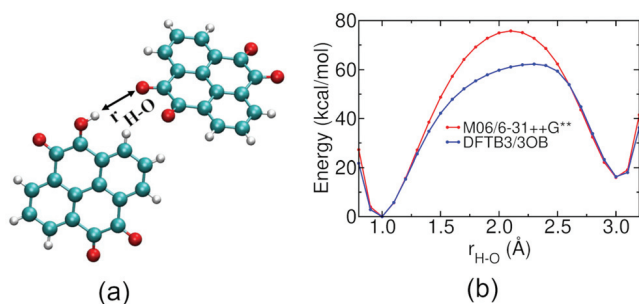

Fig. 5 (a) Depiction of the reaction coordinate (r_{H-O}) for the study of proton transfer between PTO molecules, (b) energy profile for proton transfer between two neutral PTO molecules kept frozen at their geometry in the experimental crystal structure. The shortest O–O distance between the PTO molecules is ~4 Å.

the energy profile for PT between two PTO molecules at their crystal structure geometry (Fig. 5a and b). At the large O–O distance of 4 Å, which is the shortest O–O distance between neighboring PTO molecules in crystalline PTO, M06 predicts a barrier of ~76 kcal mol^{-1} and DFTB3 underestimates the barrier by ~14 kcal mol^{-1}. DFTB3 also predicts the energy maximum to be at a distance ~0.2 Å longer than that predicted by M06. Overall, Fig. 4 and 5 highlight the deficiency of DFTB3 in describing PT between quinones at the long O–O distances typically observed in the crystal structures of quinones. The large PT barriers at these distances indicate that PT between quinone molecules in crystals is unlikely to occur in the absence of crystal distortions that reduce O–O distances or water molecules that can mediate PT. The coupling of electron transfer to PT and proton tunneling are also expected to lower the barriers. The role of these factors in mediating PT in crystalline quinones remains a topic for future investigations.

The effect of including implicit solvent for two of the above systems was also examined. For PT between a neutral PTO molecule and a hydronium ion (Fig. 2a), inclusion of solvent stabilizes the hydronium ion in both M06 and DFTB3 calculations (Fig. S17, ESI†). However, as observed before in gas phase calculations, DFTB3 over-stabilizes the proton on PTO. For proton transfer between two neutral BQ molecules with the

donor O-acceptor O distance fixed at 3.52 Å (Fig. 4a), the PT energy profile remains qualitatively similar in the gas phase and in implicit solvent, with solvation raising the energy barrier by 2.6–2.8 kcal mol^{-1} in M06 calculations and 1.4 kcal mol^{-1} in DFTB3 calculations (Table S4, ESI†).

To analyze further the errors in describing PT with DFTB3, the above two systems were also investigated using the PBE, B3LYP and ωB97XD functionals. For PT between a neutral PTO molecule and a hydronium ion (Fig. 2a), the PT energy profile is very similar for all functionals except PBE (Fig. 6a). PBE predicts the energy minimum to be closer to the hydronium O atom and PT to this O atom to be more favorable than the other functionals. On the other hand, DFTB3 predicts the energy minimum to be farther from the hydronium O atom and PT to the hydronium O atom to be less favorable than all the tested DFT functionals. For proton transfer between two neutral BQ molecules with the donor O-acceptor O distance fixed at 3.52 Å (Fig. 4a), the PT energy profile remains qualitatively the same with different functionals (Fig. 6b). The PT barrier from ωB97XD, 51.6 kcal mol^{-1}, is very similar to that from M06, 50.4 kcal mol^{-1}. B3LYP and PBE yield PT barriers of 47.4 and 39.1 kcal mol^{-1} which are higher and lower, respectively, than the DFTB3 barrier of 42.8 kcal mol^{-1}.

Overall, these results indicate that for PT between quinone and water, the errors in DFTB3 are in an opposite direction compared to the errors in PBE, and are hence not a consequence of the fact that DFTB3 is largely based off PBE. The errors in DFTB3 for PT between quinone and water are correlated with the errors in DFTB3 for the proton affinity of quinones and water, which leads to an overstabilization of protonated quinones. These proton affinity errors do not affect the PT between two quinone molecules, in which case DFTB3 results are closer to PBE results.

3. Band structure

Band structure calculations are important as they provide an understanding of the electronic properties of a solid material. Quinones can be classified as n-type semiconductors since they first undergo reduction and then combine with counterions
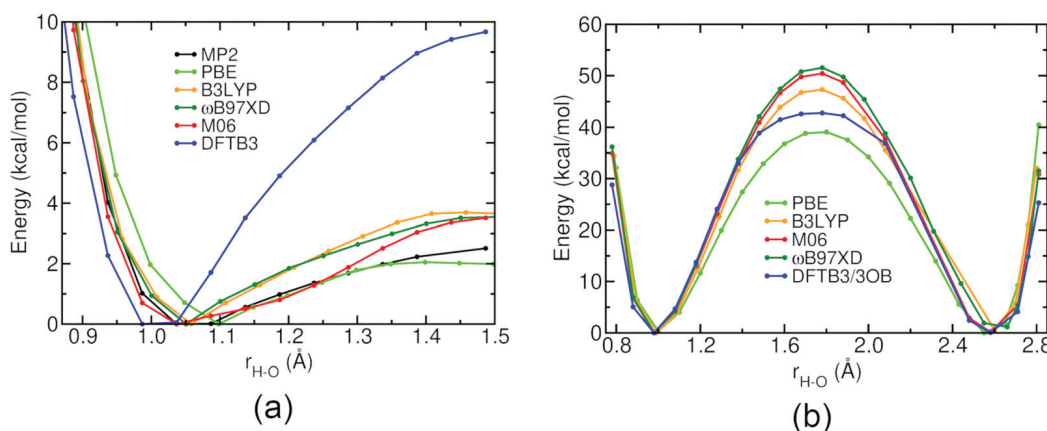
This journal is © the Owner Societies 2022

Phys. Chem. Chem. Phys., 2022, **24**, 6742–6756 | **6749**

Fig. 6 Energy profile for proton transfer between (a) a neutral PTO molecule and a hydronium ion in the gas phase, and (b) two neutral BQ molecules in the gas phase with the donor O-acceptor O distance fixed at 3.52 Å computed using different methods: MP2/aug-cc-pVDZ, PBE/6-31++G**, B3LYP/6-31++G**, ωB97XD/6-31++G**, M06/6-31++G** and DFTB3/3OB.

like Li⁺, H⁺ or Na⁺.[107] Organic molecular crystals are known to have a fundamental band gap of ∼2.0–6.0 eV between the highest occupied and lowest unoccupied states.[108] For organic semiconductors, an optical gap and a band/transport gap can exist. An optical gap arises from the energy of the lowest electronic transition accessible *via* absorption of a single photon whereas a band gap implies the energy difference between the top of the valence band (VB) and the bottom of the conduction band (CB).[109] Experimentally, it is relatively easy to obtain the optical gap from ultraviolet spectra of dilute solutions. However, determination of the band gap for crystalline organic systems *via* experiments is not trivial.[109] To the best of our knowledge, experimental band gap data for crystalline quinones is not available. Hence, the benchmarks of DFTB for band gaps of quinones need to be carried out against higher level electronic structure methods.

Over the years, DFTB has been used to predict the band structure and band gaps of different crystalline systems and it has been shown to be in fair agreement with GGA functionals like PBE. In previous work on homoatomic and heteroatomic crystalline systems, Wahiduzzaman *et al.*[110] found DFTB with scalar relativistic corrections (ZORA) and numerical atomic orbitals (NAO) to yield band structures in good agreement with PBE/TZP-ZORA. Grundkötter-Stock and co-workers[111] studied the electronic band structure for α-rhombohedral boron, two-dimensional boron sheets and boron nanotubes using the SCC-DFTB method with the *mio* parameter set meant for biological and organic molecules. In their study, PBE/PAW and SCC-DFTB showed qualitative agreement in the predicted band gap, with SCC-DFTB giving a value close to the experimental value even though both methods underestimated the band gap. SCC-DFTB/*mio* was able to reproduce the band structure close to the Fermi energy when compared to PBE/PAW. However, bands with an energy of more than 2 eV above the Fermi energy had deviations due to the underestimation of the hopping integrals in the DFTB method. Due to the small basis set used in SCC-DFTB, it showed fewer conduction bands than PBE/PAW.

GGA and local density approximation (LDA) functionals are known to underestimate the electronic band gap especially for most semiconductors[112] whereas hybrid functionals are known to give a better estimate of the band gap due to the inclusion of approximate derivative discontinuity.[113] A benchmark of hybrid functionals on semiconductors and insulators carried out by Garza *et al.*[114] showed that the HSE06 functional provided a better description of semiconductor band gaps. The DFTB3/3OB method has not been benchmarked for the band structure of organic crystals. Here, we benchmark it for the band structure of crystalline quinones using PTO and BQ as examples (Fig. 7), and the PBE and HSE06 functionals as reference. We also report the effect of inclusion of dispersion corrections and the dependence of DFT results on the pseudopotential used.

A. Effect of dispersion corrections. Molecules in organic crystals are mainly held together by weak van der Waals forces and it has been shown that including dispersion corrections while carrying out band structure calculations leads to lattice parameters and band gap values that are close to experimental values.[115] PTO was chosen as an example for the investigation of the effect of inclusion of dispersion corrections on the lattice
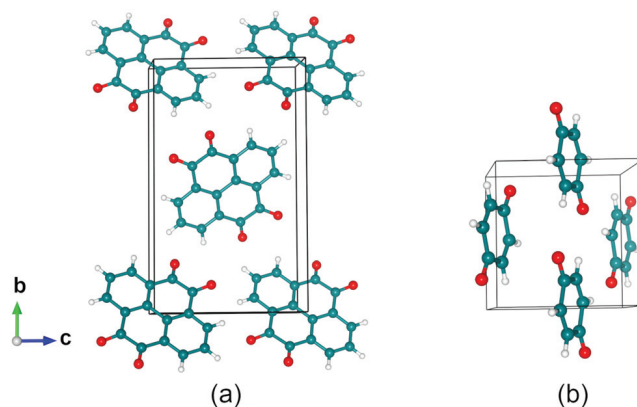

Fig. 7 Experimental crystal structures of (a) PTO[65] and (b) BQ.[66]

6750 | *Phys. Chem. Chem. Phys.*, 2022, **24**, 6742–6756

This journal is © the Owner Societies 2022

Table 5 Effect of dispersion on the calculated lattice parameters for the PTO unit cell

Method	Lattice constants (Å)			Unit cell angles (°)		
	a	b	c	α	β	γ
Experiment	3.728	15.400	9.235	90.00	100.42	90.00
PBE/PAW-D3	3.715	15.399	9.246	90.00	100.02	90.00
PBE/PAW	4.357	15.449	9.525	90.00	101.70	90.00
DFTB3-D3	3.565	14.865	8.983	90.00	98.84	90.00
DFTB3	4.143	15.276	9.031	90.00	98.04	90.01

Table 6 Effect of dispersion on the calculated band gap for crystalline PTO

Method	Band gap (eV)
PBE/PAW	1.27
DFTB3	1.29
PBE/PAW-D3	1.14
DFTB3-D3	1.14

parameters and the band structure of crystalline quinones. The lattice and geometry were optimized with and without the inclusion of dispersion corrections (D3) using both PBE/PAW and DFTB3/3OB (Table 5). The importance of the inclusion of dispersion corrections is evident in the overestimation of lattice constants, especially a, by PBE/PAW and DFTB3 without dispersion corrections, with PBE/PAW performing worse.

The band gap is determined by the energy difference between the highest energy state in the VB and the lowest energy state in the CB. With both PBE/PAW and DFTB3 (Fig. 8a and b), the band gap is indirect in nature and is determined by the energy difference between the maximum energy point of the VB at point Γ and the minimum energy point of the CB at points B–Γ. With the dispersion correction (Fig. 8c and d), the band gap is direct in nature for both methods and is defined by the highest energy point of the VB at point Γ and the lowest

energy point of the CB at point Γ. Besides affecting the nature of the band gap (direct or indirect), dispersion is found to lead to slight lowering of the band energies for both PBE/PAW and DFTB3 (Fig. 8). The partial density of states (PDOS) plots remain largely unaffected by dispersion. Dispersion also leads to lowering of the band gap by $\sim$0.13 eV for both PBE/PAW and DFTB3 (Table 6).

B. Effect of different pseudopotentials. We benchmarked USPP, the ONCV PP and the PAW method with the PBE functional in order to choose a well-tuned PP that is transferable and can describe the structure and band structure/energies for crystalline quinones well.[116] For PTO, PBE-D3 with the PAW method and USPP yields lattice parameters in close agreement with experiment (Table 7). However, even with dispersion corrections, PBE/ONCV underestimates the lattice constants compared to experiment. PAW and USPP predict a direct band gap of 1.14 eV obtained from the highest point of the VB at point Γ and the lowest point of the CB at point Γ
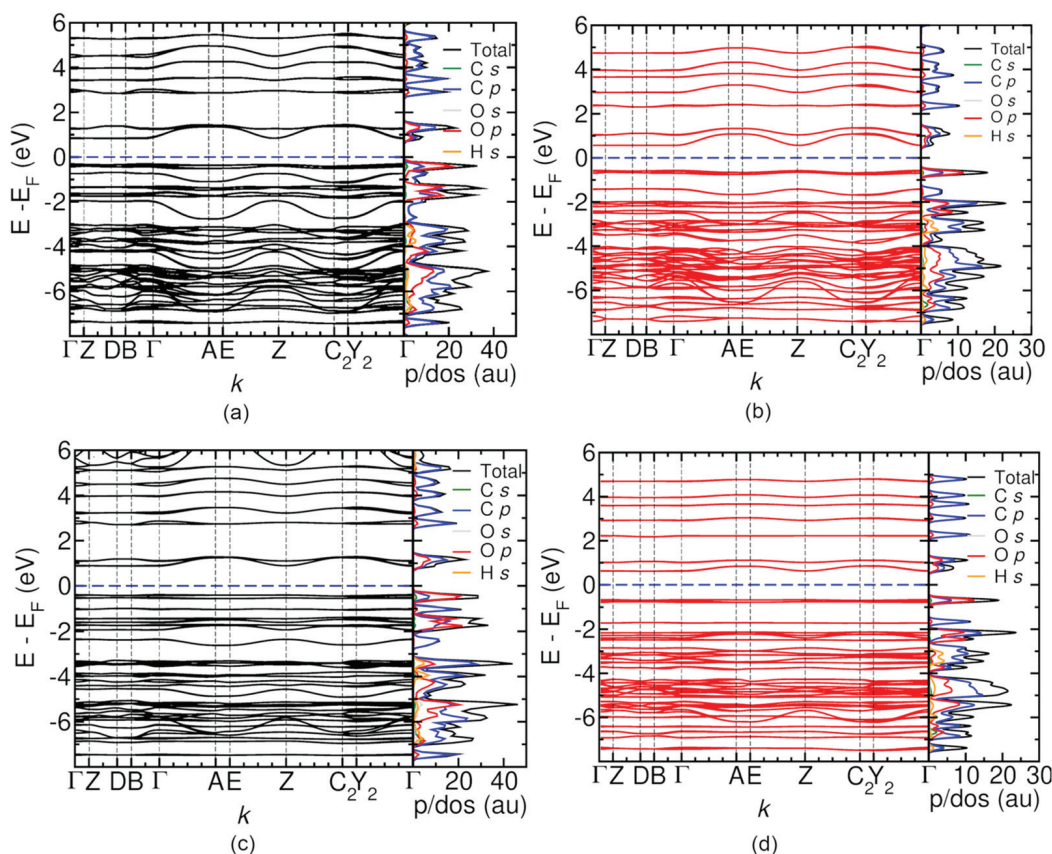

Fig. 8 A comparison of the calculated band structure and partial/total density of states for PTO along the $\Gamma-Z-D-B-\Gamma-A-E-Z-C_2-Y_2-\Gamma$ k-path. The Fermi level is highlighted in blue for easy visualization. (a) PBE/PAW, (b) DFTB3, (c) PBE/PAW-D3 and (d) DFTB3-D3.

This journal is © the Owner Societies 2022

Phys. Chem. Chem. Phys., 2022, **24**, 6742–6756 | **6751**

Table 7 Effect of pseudopotential on the calculated lattice parameters for the PTO unit cell

Method	Lattice constants (Å)			Unit cell angles (°)		
	a	b	c	α	β	γ
Experiment	3.728	15.400	9.235	90.00	100.42	90.00
PBE/PAW-D3	3.715	15.399	9.246	90.00	100.02	90.00
PBE/USPP-D3	3.709	15.388	9.237	90.00	100.00	90.00
PBE/ONCV-D3	3.525	14.745	8.903	90.00	99.60	90.00
DFTB3-D3	3.565	14.865	8.983	90.00	98.84	90.00

Table 8 Effect of different pseudopotentials on the band gap of PTO and BQ. The PBE functional and D3 dispersion correction were used in all calculations. ONCV//PAW indicates a PBE/ONCV single point calculation at a PBE/PAW-optimized lattice-geometry

Method	PTO band gap (eV)	BQ band gap (eV)
PAW	1.14	1.28
USPP	1.14	1.27
ONCV	1.00	1.15
ONCV//PAW	1.14	1.28

(Table 8 and Fig. S18, ESI†). The ONCV PP yields a band gap ∼0.14 eV lower in energy compared to the other pseudopotentials. The ONCV PP yields a band gap of 1.14 eV with a PAW-optimized lattice geometry, indicating that the ONCV PP can predict a band gap in agreement with PAW and USPP if the geometry is accurate. Similar trends are observed for BQ (Tables 8 and 9). Overall, we conclude that different

Table 9 Effect of pseudopotential on the calculated lattice parameters for the BQ unit cell

Method	Lattice constants (Å)			Unit cell angles (°)		
	a	b	c	α	β	γ
Experiment[66]	5.743	6.771	6.867	90.00	100.14	90.00
PBE/PAW-D3	5.756	6.647	6.773	90.00	99.84	90.00
PBE/USPP-D3	5.748	6.642	6.763	90.00	99.82	90.00
PBE/ONCV-D3	5.428	6.483	6.326	90.00	97.42	90.00
DFTB3-D3	5.480	6.476	6.299	89.26	95.19	90.72

pseudopotentials have no effect on the fundamental band gap for crystalline quinones provided the geometries and lattice parameters are similar.

C. Comparison between PBE and DFTB. For lattice-geometry optimizations, DFTB3-D3 is found to be only as good as PBE/ONCV-D3, with the lattice constants shorter by 0.2–0.5 Å compared to experiment (Tables 7 and 9). For PTO, the band structure obtained from DFTB3-D3 differs slightly from the one predicted by PBE/PAW-D3 (Fig. 8c and d). DFTB3-D3 fails to reproduce the bands at energies more than 2 eV higher than the Fermi energy when compared to PBE/PAW-D3. This is attributed to the minimal basis set used in the DFTB3 method.[111] As shown in Table 6, PBE/PAW-D3 and DFTB3-D3 are in excellent agreement in terms of the predicted band gap values. Both PBE/PAW-D3 and DFTB3-D3 show good qualitative agreement in the PDOS for PTO (Fig. 8c and d). With both methods, the energy levels in the VB closer to the Fermi level have dominant contributions from O p orbitals, with smaller contributions from C p orbitals and C s orbitals. The energy levels in the CB closer to the Fermi level have dominant contributions from C p orbitals, with smaller contributions from O p orbitals.

For BQ, PBE/PAW-D3 predicts an indirect band gap of 1.28 eV (Fig. 9) given by the energy difference between the highest point of the VB at point C_2 and the lowest point of the CB at points B–Γ. For DFTB3-D3, the indirect band gap of 1.23 eV is between the highest point of the VB at point Z and the lowest point of the CB at point Γ. Even though the bands obtained using DFTB3-D3 are slightly shifted to higher energies in the VB band compared to PBE/PAW-D3, the band structures from the two methods are in good qualitative agreement. The VB and CB for BQ are comprised of the same orbitals as described earlier for PTO. The calculated band gap for BQ is higher than that of PTO (Table 8), indicating that PTO may have a higher capacity utilization due to its smaller band gap.[85]

D. Effect of different functionals. Many studies done on solid state band gaps show that GGA and LDA functionals are computationally affordable but underestimate the band gap.[111,112] Hybrid functionals and Green's function methods
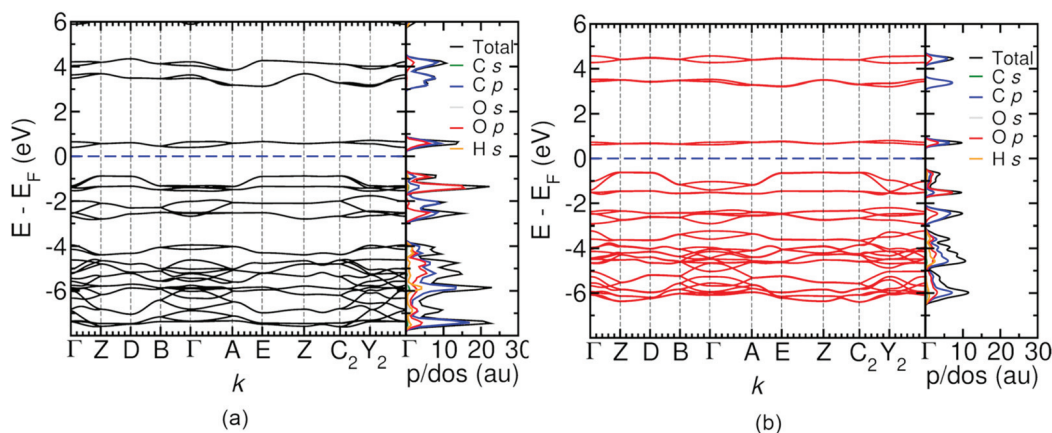

Fig. 9 A comparison of the calculated band structure and partial/total density of states for BQ along the Γ–Z–D–B–Γ–A–E–Z–C_2–Y_2–Γ k-path. The Fermi level is highlighted in blue for easy visualization. (a) PBE/PAW-D3, (b) DFTB3-D3.

6752 | *Phys. Chem. Chem. Phys.*, 2022, **24**, 6742–6756

This journal is © the Owner Societies 2022

Table 10 Calculated gas phase H–L gaps for PTO and BQ molecules using GGA and hybrid functionals

Molecule	HOMO–LUMO gap (eV)		
	PBE	B3LYP	HSE06
PTO	1.45	3.50	3.15
BQ	1.71	3.84	3.50

provide a better description of band gaps when compared to experiments, with the latter being computationally expensive.[113] In our study, we chose to use the HSE06 functional since it has been cited to have excellent agreement with experimental band gap energies for organic polymer crystals.[117] Organic molecular crystals are known to have a fundamental band gap of $\sim$2.0–6.0 eV,[108] and due to the lack of experimental band gap data for quinones, we used this range to gauge the accuracy of our computed results. We utilized the geometry and lattice parameters optimized using PBE/PAW-D3 and calculated the band gap using HSE06/ONCV-D3. The band gaps for crystalline PTO and BQ obtained using the HSE06 functional are 2.31 eV and 2.93 eV (Fig. S19, ESI†), respectively, and fall within the experimentally known range for the band gap of organic molecular crystals. These band gaps are higher than the PBE and DFTB3 band gaps listed in Tables 6 and 8. Gas phase HOMO–LUMO (H–L) gaps for PTO and BQ molecules with the PBE, B3LYP and HSE06 functionals and the 6-31+G** basis set show similar trends (Table 10). The hybrid functionals raise the H-L gap compared to PBE.

Conclusions

The computational investigation of charge transport in crystalline quinones requires methods that can accurately model the various redox states of quinones and are computationally efficient. The semi-empirical DFTB3 method is promising in terms of computational speed but needs to be benchmarked for its accuracy in describing charge transport in quinones. We find that DFTB3 with the 3OB parameter set yields an accurate description of the qualitative trends in the reduction potentials of *o*- and *p*-quinones in aqueous solution. Using an implicit solvation model, the reduction potentials predicted by DFTB3 are lower than those from DFT. DFTB3 with explicit water in a QM/MM framework yields reduction potential values lower than DFT and DFTB3 with implicit solvent. With either solvation model, DFTB3 underestimates the reduction potentials only by less than $\sim$2.5 kcal mol^{-1}. We conclude that DFTB3 is sufficiently accurate for studying the reduction of quinones in aqueous solution modeled implicitly or explicitly.

The PT and PA calculations indicate the inability of DFTB3 to describe the PA of quinones accurately. For both neutral and singly reduced *o*-BQ and *p*-BQ, DFTB3 overestimates the PA by $\sim$7–10 kcal mol^{-1}. At long O–O distances between quinones, the PT barriers are underestimated by more than 10 kcal mol^{-1} by DFTB3, highlighting the deficiency of DFTB3 in describing PT between quinones at long distances typically observed in

crystal structures. The large PT barriers ($\sim$50–75 kcal mol^{-1}) indicate the possibility that water molecules, crystal distortions, proton tunneling or coupling of electron transfer to PT may be involved in facilitating PT in crystalline quinones.

Band structure and band gap calculations reveal DFTB3 to be in very good agreement with PBE/PAW. However, both DFTB3 and PBE underestimate the band gap when compared to the HSE06 functional which predicts band gaps within the experimentally known range for organic molecular crystals. Inclusion of dispersion was found to be important to avoid overestimation of lattice constants and was found to have a small lowering effect on the band energies and the band gap.

Overall, this study highlights the need for further development and/or reparameterization of DFTB for describing PT involving quinone molecules and the band structure of crystalline quinones. Recent studies in the literature have shown that fitting the repulsive potential, the Hubbard parameter (chemical hardness) and the empirical parameter ζ, which describes the interaction of hydrogen with other atoms, leads to a better description of proton affinities.[21,95] Reparameterization efforts for improved band structure and band gap of solid materials have also been reported.[110,118] Several recent developments of DFTB such as long range-corrected DFTB[23] and GFN-xTB[25,119] remain to be tested for the description of charge storage/transport in quinones. Overall, our work lays the foundation for further development/parameterization of the DFTB method so that a proper description of the different properties related to charge storage/transport in crystalline quinones in batteries can be achieved. A sufficiently accurate version of DFTB will help effective modeling of the dynamics of charge transport in crystalline quinones.

Author contributions

P. G. designed research. M. K., M. R, and J. Z. carried out research. M. K. and P. G. wrote the paper. Y. Y. contributed to revision.

Conflicts of interest

There are no conflicts to declare.

Acknowledgements

This journal is © the Owner Societies 2022

Phys. Chem. Chem. Phys., 2022, **24**, 6742–6756 | **6753**

References

1 D. Larcher and J. M. Tarascon, *Nat. Chem.*, 2015, **7**, 19–29.

2 P. Poizot, J. Gaubicher, S. Renault, L. Dubois, Y. Liang and Y. Yao, *Chem. Rev.*, 2020, **120**, 6490–6557.

3 C. Han, H. Li, R. Shi, T. Zhang, J. Tong, J. Li and B. Li, *J. Mater. Chem. A*, 2019, **7**, 23378–23415.

4 E. J. Son, J. H. Kim, K. Kim and C. B. Park, *J. Mater. Chem. A*, 2016, **4**, 11179–11202.

5 T. B. Schon, B. T. McAllister, P.-F. Li and D. S. Seferos, *Chem. Soc. Rev.*, 2016, **45**, 6345–6404.

6 Z. Song and H. Zhou, *Energy Environ. Sci.*, 2013, **6**, 2280–2301.

7 D. L. Williams, J. J. Byrne and J. S. Driscoll, *J. Electrochem. Soc.*, 1969, **116**, 2.

8 H. Dong, O. Tutusaus, Y. Liang, Y. Zhang, Z. Lebens-Higgins, W. Yang, R. Mohtadi and Y. Yao, *Nat. Energy*, 2020, **5**, 1043–1050.

9 J. Zhang, Z. Chen, Q. Ai, T. Terlier, F. Hao, Y. Liang, H. Guo, J. Lou and Y. Yao, *Joule*, 2021, **5**, 1845–1859.

10 F. Hao, Y. Liang, Y. Zhang, Z. Chen, J. Zhang, Q. Ai, H. Guo, Z. Fan, J. Lou and Y. Yao, *ACS Energy Lett.*, 2021, **6**, 201–207.

11 Y. Liang, Y. Jing, S. Gheytani, K.-Y. Lee, P. Liu, A. Facchetti and Y. Yao, *Nat. Mater.*, 2017, **16**, 841–848.

12 Z. Guo, J. Huang, X. Dong, Y. Xia, L. Yan, Z. Wang and Y. Wang, *Nat. Commun.*, 2020, **11**, 959.

13 R. Emanuelsson, M. Sterby, M. Strømme and M. Sjödin, *J. Am. Chem. Soc.*, 2017, **139**, 4828–4834.

14 H. Wang, R. Emanuelsson, C. Karlsson, P. Jannasch, M. Strømme and M. Sjödin, *ACS Appl. Mater. Interfaces*, 2021, **13**, 19099–19108.

15 C. Strietzel, M. Sterby, H. Huang, M. Strømme, R. Emanuelsson and M. Sjödin, *Angew. Chem., Int. Ed.*, 2020, **59**, 9631–9638.

16 F. Spiegelman, N. Tarrat, J. Cuny, L. Dontot, E. Posenitskiy, C. Martí, A. Simon and M. Rapacioli, *Adv. Phys.: X*, 2020, **5**, 1710252.

17 B. Hourahine, B. Aradi, V. Blum, F. Bonafe, A. Buccheri, C. Camacho, C. Cevallos, M. Y. Deshaye, T. Dumitrica, A. Dominguez, S. Ehlert, M. Elstner, T. van der Heide, J. Hermann, S. Irle, J. J. Kranz, C. Kohler, T. Kowalczyk, T. Kubar, I. S. Lee, V. Lutsker, R. J. Maurer, S. K. Min, I. Mitchell, C. Negre, T. A. Niehaus, A. M. N. Niklasson, A. J. Page, A. Pecchia, G. Penazzi, M. P. Persson, J. Rezac, C. G. Sanchez, M. Sternberg, M. Stohr, F. Stuckenberg, A. Tkatchenko, V. W. Yu and T. Frauenheim, *J. Chem. Phys.*, 2020, **152**, 124101.

18 S. I. Allec, Y. Sun, J. Sun, C.-E. A. Chang and B. M. Wong, *J. Chem. Theory Comput.*, 2019, **15**, 2807–2815.

19 C. P. Chou, A. W. Sakti, Y. Nishimura and H. Nakai, *Chem. Rec.*, 2019, **19**, 746–757.

20 Y. Nishimura and H. Nakai, *J. Comput. Chem.*, 2019, **40**, 1538–1549.

21 M. Gaus, Q. Cui and M. Elstner, *J. Chem. Theory Comput.*, 2011, **7**, 931–948.

22 M. Gaus, A. Goez and M. Elstner, *J. Chem. Theory Comput.*, 2013, **9**, 338–354.

23 V. Q. Vong, J. A. Kuriappan, M. Kubillus, J. J. Kranz, T. Mast, T. A. Niehaus, S. Irle and M. Elstner, *J. Chem. Theory Comput.*, 2018, **14**, 115–125.

24 A. S. Christensen, M. Elstner and Q. Cui, *J. Chem. Phys.*, 2015, **143**, 084123.

25 C. Bannwarth, S. Ehlert and S. Grimme, *J. Chem. Theory Comput.*, 2019, **15**, 1652–1671.

26 M. Mortazavi, J. G. Brandenburg, R. J. Maurer and A. Tkatchenko, *J. Phys. Chem. Lett.*, 2018, **9**, 399–405.

27 J. G. Brandenburg and S. Grimme, *J. Phys. Chem. Lett.*, 2014, **5**, 1785–1789.

28 G. A. Dolgonos and A. D. Boese, *Chem. Phys. Lett.*, 2019, **718**, 7–11.

29 A. D. Vito, A. Pecchia, M. A. D. Maur and A. D. Carlo, Tight binding parameterization through particle swarm optimization algorithm, 2020 International Conference on Numerical Simulation of Optoelectronic Devices (NUSOD), 2020.

30 N. F. Aguirre, A. Morgenstern, M. J. Cawkwell, E. R. Batista and P. Yang, *J. Chem. Theory Comput.*, 2020, **16**, 1469–1481.

31 C. Panosetti, A. Engelmann, L. Nemec, K. Reuter and J. T. Margraf, *J. Chem. Theory Comput.*, 2020, **16**, 2181–2191.

32 A. W. Huran, C. Steigemann, T. Frauenheim, B. Aradi and M. A. L. Marques, *J. Chem. Theory Comput.*, 2018, **14**, 2947–2954.

33 G. R. Jenness, C. G. Bresnahan and M. K. Shukla, *J. Chem. Theory Comput.*, 2020, **16**, 6894–6903.

34 J. M. Knaup, B. Hourahine and T. Frauenheim, *J. Phys. Chem. A*, 2007, **111**, 5637–5641.

35 Z. Bodrog, B. Aradi and T. Frauenheim, *J. Chem. Theory Comput.*, 2011, **7**, 2654–2664.

36 N. Goldman, K. E. Kweon, B. Sadigh, T. W. Heo, R. K. Lindsey, C. H. Pham, L. E. Fried, B. Aradi, K. Holliday, J. R. Jeffries and B. C. Wood, *J. Chem. Theory Comput.*, 2021, **17**, 4435–4448.

37 M. P. Lourenço, M. C. da Silva, A. F. Oliveira, M. C. Quintão and H. A. Duarte, *Theor. Chem. Acc.*, 2016, **135**, 250.

38 Y. Jing, Y. Liang, S. Gheytani and Y. Yao, *Nano Energy*, 2017, **37**, 46–52.

39 Y. Yao and Y. Liang, *Gen. Chem.*, 2017, **3**, 207–212.

6754 | *Phys. Chem. Chem. Phys.*, 2022, **24**, 6742–6756

This journal is © the Owner Societies 2022

40 Y. Liang and Y. Yao, *Joule*, 2018, **2**, 1690–1706.

41 X. Chi, Y. Liang, F. Hao, Y. Zhang, J. Whiteley, H. Dong, P. Hu, S. Lee and Y. Yao, *Angew. Chem., Int. Ed.*, 2018, **57**, 2630–2634.

42 F. Hao, X. Chi, Y. Liang, Y. Zhang, R. Xu, H. Guo, T. Terlier, H. Dong, K. Zhao, J. Lou and Y. Yao, *Joule*, 2019, **3**, 1349–1359.

43 X. Chi, F. Hao, J. Zhang, X. Wu, Y. Zhang, S. Gheytani, Z. Wen and Y. Yao, *Nano Energy*, 2019, **62**, 718–724.

44 Y. Zhang, Y. Liang, H. Dong, X. Wang and Y. Yao, *J. Electrochem. Soc.*, 2020, **167**, 070558.

45 Y. Jing, Y. Liang, S. Gheytani and Y. Yao, *ChemSusChem*, 2020, **13**, 2250–2255.

46 A. D. Becke, *J. Chem. Phys.*, 1993, **98**, 1372–1377.

47 M. J. Frisch, J. A. Pople and J. S. Binkley, *J. Chem. Phys.*, 1984, **80**, 3265–3269.

48 M. T. Huynh, C. W. Anson, A. C. Cavell, S. S. Stahl and S. Hammes-Schiffer, *J. Am. Chem. Soc.*, 2016, **138**, 15903–15910.

49 M. Cossi, N. Rega, G. Scalmani and V. Barone, *J. Comput. Chem.*, 2003, **24**, 669–681.

50 M. J. Frisch, G. W. Trucks, H. B. Schlegel, G. E. Scuseria, M. A. Robb, J. R. Cheeseman, G. Scalmani, V. Barone, G. A. Petersson, H. Nakatsuji, X. Li, M. Caricato, A. Marenich, J. Bloino, B. G. Janesko, R. Gomperts, B. Mennucci, H. P. Hratchian, J. V. Ortiz, A. F. Izmaylov, J. L. Sonnenberg, D. Williams-Young, F. L. F. Ding, F. Egidi, J. Goings, B. Peng, A. Petrone, T. Henderson, D. Ranasinghe, V. G. Zakrzewski, J. Gao, N. Rega, G. Zheng, W. Liang, M. Hada, M. Ehara, K. Toyota, R. Fukuda, J. Hasegawa, M. Ishida, T. Nakajima, Y. Honda, O. Kitao, H. Nakai, T. Vreven, J. J. A. Montgomery, J. E. Peralta, F. Ogliaro, M. Bearpark, J. J. Heyd, E. Brothers, K. N. Kudin, V. N. Staroverov, T. Keith, R. Kobayashi, K. Raghavachari, A. Rendell, J. C. Burant, S. S. Iyengar, J. Tomasi, M. Cossi, J. M. Millam, M. Klene, C. Adamo, J. W. O. R. Cammi, R. L. Martin, K. Morokuma, O. Farkas, J. B. Foresman and D. J. Fox, *Gaussian 09, Revision E.01*, Gaussian, Inc, Wallingford CT, 2013.

51 B. R. Brooks, C. L. Brooks, 3rd, A. D. Mackerell, Jr., L. Nilsson, R. J. Petrella, B. Roux, Y. Won, G. Archontis, C. Bartels, S. Boresch, A. Caflisch, L. Caves, Q. Cui, A. R. Dinner, M. Feig, S. Fischer, J. Gao, M. Hodoscek, W. Im, K. Kuczera, T. Lazaridis, J. Ma, V. Ovchinnikov, E. Paci, R. W. Pastor, C. B. Post, J. Z. Pu, M. Schaefer, B. Tidor, R. M. Venable, H. L. Woodcock, X. Wu, W. Yang, D. M. York and M. Karplus, *J. Comput. Chem.*, 2009, **30**, 1545–1614.

52 A. D. MacKerell, D. Bashford, M. Bellott, R. L. Dunbrack, J. D. Evanseck, M. J. Field, S. Fischer, J. Gao, H. Guo, S. Ha, D. Joseph-McCarthy, L. Kuchnir, K. Kuczera, F. T. K. Lau, C. Mattos, S. Michnick, T. Ngo, D. T. Nguyen, B. Prodhom, W. E. Reiher, B. Roux, M. Schlenkrich, J. C. Smith, R. Stote, J. Straub, M. Watanabe, J. Wiórkiewicz-Kuczera, D. Yin and M. Karplus, *J. Phys. Chem. B*, 1998, **102**, 3586–3616.

53 K. Vanommeslaeghe, E. Hatcher, C. Acharya, S. Kundu, S. Zhong, J. Shim, E. Darian, O. Guvench, P. Lopes, I. Vorobyov and A. D. Mackerell, Jr., *J. Comput. Chem.*, 2010, **31**, 671–690.

54 A. Klamt and G. Schüürmann, *J. Chem. Soc., Perkin Trans. 2*, 1993, 799–805.

55 M. Mantina, A. C. Chamberlin, R. Valero, C. J. Cramer and D. G. Truhlar, *J. Phys. Chem. A*, 2009, **113**, 5806–5812.

56 S. Grimme, J. Antony, S. Ehrlich and H. Krieg, *J. Chem. Phys.*, 2010, **132**, 154104.

57 S. Grimme, S. Ehrlich and L. Goerigk, *J. Comput. Chem.*, 2011, **32**, 1456–1465.

58 M. Kubillus, T. Kubar, M. Gaus, J. Rezac and M. Elstner, *J. Chem. Theory Comput.*, 2015, **11**, 332–342.

59 Y. Zhao and D. G. Truhlar, *Theor. Chem. Acc.*, 2007, **120**, 215–241.

60 C. Møller and M. S. Plesset, *Phys. Rev.*, 1934, **46**, 618–622.

61 A. K. Wilson, D. E. Woon, K. A. Peterson and T. H. Dunning, *J. Chem. Phys.*, 1999, **110**, 7667–7676.

62 A. G. Baboul, L. A. Curtiss, P. C. Redfern and K. Raghavachari, *J. Chem. Phys.*, 1999, **110**, 7650.

63 L. A. Curtiss, K. Raghavachari, P. C. Redfern, V. Rassolov and J. A. Pople, *J. Chem. Phys.*, 1998, **109**, 7764–7776.

64 B. Aradi, B. Hourahine and T. Frauenheim, *J. Phys. Chem. A*, 2007, **111**, 5678–5684.

65 J. Zhang, M. Kitheka, E. Kamphaus, M. Ren, Y. Zhang, Y. Jing, H. Dong, Y. Liang, J. Tour, P. B. Balbuena, P. Goyal and Y. Yao, unpublished work.

66 C. R. Groom, I. J. Bruno, M. P. Lightfoot and S. C. Ward, *Acta Crystallogr., Sect. B: Struct. Sci., Cryst. Eng. Mater.*, 2016, **72**, 171–179.

67 K. B. John, P. Perdew and M. Ernzerhof, *Phys. Rev. Lett.*, 1997, **78**, 1396.

68 J. Heyd and G. E. Scuseria, *J. Chem. Phys.*, 2004, **121**, 1187–1192.

69 P. E. Blochl, *Phys. Rev. B: Condens. Matter Mater. Phys.*, 1994, **50**, 17953–17979.

70 D. Vanderbilt, *Phys. Rev. B: Condens. Matter Mater. Phys.*, 1990, **41**, 7892–7895.

71 D. R. Hamann, *Phys. Rev. B: Condens. Matter Mater. Phys.*, 2013, **88**, 085117.

72 G. Prandini, A. Marrazzo, I. E. Castelli, N. Mounet and N. Marzari, *npj Comput. Mater.*, 2018, **4**, 72.

73 A. Dal Corso, *Comput. Mater. Sci.*, 2014, **95**, 337–350.

74 M. Schlipf and F. Gygi, *Comput. Phys. Commun.*, 2015, **196**, 36–44.

75 P. Giannozzi, O. Baseggio, P. Bonfa, D. Brunato, R. Car, I. Carnimeo, C. Cavazzoni, S. de Gironcoli, P. Delugas, F. Ferrari Ruffino, A. Ferretti, N. Marzari, I. Timrov, A. Urru and S. Baroni, *J. Chem. Phys.*, 2020, **152**, 154105.

76 H. J. Monkhorst and J. D. Pack, *Phys. Rev. B: Condens. Matter Mater. Phys.*, 1976, **13**, 5188–5192.

77 Y. Hinuma, G. Pizzi, Y. Kumagai, F. Oba and I. Tanaka, *Comput. Mater. Sci.*, 2017, **128**, 140–184.

78 R. Fletcher, *Practical Methods of Optimization*, John Wiley and Sons, 1987.

79 J. R. Shewchuk, 1994.

80 G. Pizzi, V. Vitale, R. Arita, S. Blügel, F. Freimuth, G. Géranton, M. Gibertini, D. Gresch, C. Johnson,

This journal is © the Owner Societies 2022

Phys. Chem. Chem. Phys., 2022, **24**, 6742–6756 | **6755**

T. Koretsune, J. Ibañez-Azpiroz, H. Lee, J.-M. Lihm, D. Marchand, A. Marrazzo, Y. Mokrousov, J. I. Mustafa, Y. Nohara, Y. Nomura, L. Paulatto, S. Poncé, T. Ponweiser, J. Qiao, F. Thöle, S. S. Tsirkin, M. Wierzbowska, N. Marzari, D. Vanderbilt, I. Souza, A. A. Mostofi and J. R. Yates, *J. Phys.: Condens. Matter*, 2020, **32**, 165902.

81 N. Marzari and D. Vanderbilt, *Phys. Rev. B: Condens. Matter Mater. Phys.*, 1997, **56**, 12847–12865.

82 S. Er, C. Suh, M. P. Marshak and A. Aspuru-Guzik, *Chem. Sci.*, 2015, **6**, 885–893.

83 D. P. Tabor, R. Gómez-Bombarelli, L. Tong, R. G. Gordon, M. J. Aziz and A. Aspuru-Guzik, *J. Mater. Chem. A*, 2019, **7**, 12833–12841.

84 K. C. Kim, T. Liu, S. W. Lee and S. S. Jang, *J. Am. Chem. Soc.*, 2016, **138**, 2374–2382.

85 Y. Ding, Y. Li and G. Yu, *Chem*, 2016, **1**, 790–801.

86 G. C. Sedenho, D. De Porcellinis, Y. Jing, E. Kerr, L. M. Mejia-Mendoza, Á. Vazquez-Mayagoitia, A. Aspuru-Guzik, R. G. Gordon, F. N. Crespilho and M. J. Aziz, *ACS Appl. Energy Mater.*, 2020, **3**, 1933–1943.

87 Q. Zhang, A. Khetan and S. Er, *Sci. Rep.*, 2020, **10**, 22149.

88 X. Zhou, A. Khetan and S. Er, *Batteries*, 2021, **7**, 71.

89 G. Li, X. Zhang and Q. Cui, *J. Phys. Chem. B*, 2003, **107**, 8643–8653.

90 H. Jin, P. Goyal, A. K. Das, M. Gaus, M. Meuwly and Q. Cui, *J. Phys. Chem. B*, 2016, **120**, 1894–1910.

91 M. S. Formaneck, G. Li, X. Zhang and Q. Cui, *J. Theor. Comput. Chem.*, 2002, **01**, 53–67.

92 S. Bhattacharyya, M. T. Stankovich, D. G. Truhlar and J. Gao, *J. Phys. Chem. A*, 2007, **111**, 5729–5742.

93 H. Neugebauer, F. Bohle, M. Bursch, A. Hansen and S. Grimme, *J. Phys. Chem. A*, 2020, **124**, 7166–7176.

94 P. Goyal, N. Ghosh, P. Phatak, M. Clemens, M. Gaus, M. Elstner and Q. Cui, *J. Am. Chem. Soc.*, 2011, **133**, 14981–14997.

95 P. Goyal, M. Elstner and Q. Cui, *J. Phys. Chem. B*, 2011, **115**, 6790–6805.

96 D. Riccardi, X. Zhu, P. Goyal, S. Yang, G. Hou and Q. Cui, *Sci. China: Chem.*, 2012, **55**, 3–18.

97 P. Goyal, J. Lu, S. Yang, M. R. Gunner and Q. Cui, *Proc. Natl. Acad. Sci. U. S. A.*, 2013, **110**, 18886.

98 P. Goyal, H.-J. Qian, S. Irle, X. Lu, D. Roston, T. Mori, M. Elstner and Q. Cui, *J. Phys. Chem. B*, 2014, **118**, 11007–11027.

99 P. Goyal, S. Yang and Q. Cui, *Chem. Sci.*, 2015, **6**, 826–841.

100 Ł. Walewski, D. Krachtus, S. Fischer, J. C. Smith, P. Bała and B. Lesyng, *Int. J. Quantum Chem.*, 2006, **106**, 636–640.

101 J. Ono, M. Imai, Y. Nishimura and H. Nakai, *J. Phys. Chem. B*, 2020, **124**, 8524–8539.

102 S. Nachimuthu, J. Gao and D. G. Truhlar, *Chem. Phys.*, 2012, **400**, 8–12.

103 M. Meuwly and M. Karplus, *J. Chem. Phys.*, 2002, **116**, 2572–2585.

104 K. Kosugi, H. Nakano and H. Sato, *J. Chem. Theory Comput.*, 2019, **15**, 4965–4973.

105 P. H. König, M. Hoffmann, T. Frauenheim and Q. Cui, *J. Phys. Chem. B*, 2005, **109**, 9082–9095.

106 S. Adam and A.-N. Bondar, *PLoS One*, 2018, **13**, e0201298.

107 Y. Lu and J. Chen, *Nat. Rev. Chem.*, 2020, **4**, 127–142.

108 J. Sworakowski, *Mol. Cryst. Liq. Cryst.*, 2007, **11**, 1–11.

109 J.-L. Bredas, *Mater. Horiz.*, 2014, **1**, 17–19.

110 M. Wahiduzzaman, A. F. Oliveira, P. Philipsen, L. Zhechkov, E. van Lenthe, H. A. Witek and T. Heine, *J. Chem. Theory Comput.*, 2013, **9**, 4006–4017.

111 B. Grundkotter-Stock, V. Bezugly, J. Kunstmann, G. Cuniberti, T. Frauenheim and T. A. Niehaus, *J. Chem. Theory Comput.*, 2012, **8**, 1153–1163.

112 M. K. Chan and G. Ceder, *Phys. Rev. Lett.*, 2010, **105**, 196403.

113 A. Dittmer, R. Izsak, F. Neese and D. Maganas, *Inorg. Chem.*, 2019, **58**, 9303–9315.

114 A. J. Garza and G. E. Scuseria, *J. Phys. Chem. Lett.*, 2016, **7**, 4165–4170.

115 H. Takaba, S. Kimura and M. K. Alam, *Chem. Phys.*, 2017, **485-486**, 22–28.

116 P. Borlido, J. Doumont, F. Tran, M. A. L. Marques and S. Botti, *J. Chem. Theory Comput.*, 2020, **16**, 3620–3627.

117 M. E. Foster and K. Leong-Hau, Computational Design of Near-IR Absorbing Organic Materials for Light Harvesting Application, United States, 2016, https://www.osti.gov/servlets/purl/1364870.

118 J. Lee, S. Ganguli, A. K. Roy and S. C. Badescu, *J. Chem. Phys.*, 2019, **150**, 174706.

119 S. Grimme, C. Bannwarth and P. Shushkov, *J. Chem. Theory Comput.*, 2017, **13**, 1989–2009.

120 J. Towns, T. Cockerill, M. Dahan, I. Foster, K. Gaither, A. Grimshaw, V. Hazelwood, S. Lathrop, D. Lifka, G. D. Peterson, R. Roskies, J. R. Scott and N. Wilkins-Diehr, *Comput. Sci. Eng.*, 2014, **16**, 62–74.

121 W. Humphrey, A. Dalke and K. Schulten, *J. Mol. Graphics*, 1996, **14**, 33–38.

122 K. Momma and F. Izumi, *J. Appl. Crystallogr.*, 2011, **44**, 1272–1276.

123 T. G. D. Team GIMP, 2019, https://www.gimp.org/.

124 E. G. Stambulchik, XMGRACE, https://plasma-gate.weizmann.ac.il/Grace/.